14

Fracture Specific Stiffness: The Critical Link Between the Scaling Behavior of Hydro-Mechanical Coupling in Fractures and Seismic Monitoring

Laura J. Pyrak-Nolte[1,2,3]

[1]**Department of Physics and Astronomy, Purdue University, West Lafayette, IN, United States**
[2]**Department of Earth, Atmospheric and Planetary Sciences, Purdue University, West Lafayette, IN, United States**
[3]**Lyle School of Civil Engineering, Purdue University, West Lafayette, IN, United States**

INTRODUCTION

Sustainable and safe storage or extraction of fluids from subsurface rock depend on the ability to image and characterize fracture systems throughout the life cycle of a site. Of particular concern is the integrity of the caprock which is an impermeable geological unit (or a set of units) that prevents or minimizes leakage from deeper geologic storage sites. Typical caprocks include shale and other mudstone rock that act as natural barriers to the flow of liquids and gases because the porosity of these rocks is dominated by poorly connected nano-pores, resulting in low permeability (Ilgen et al., 2017). However, changes in the stress-field during the injection or withdrawal of fluids in a subsurface reservoir may open preexisting fractures, reactivate faults, and may initiate, grow, and coalesce new fractures. These mechanical discontinuities are potential pathways for fluids to escape through the caprock. An outstanding issue for sustained, safe geologic storage is the need for improved methods to image and characterize fracture systems throughout the life cycle of a subsurface site (Harbert et al., 2016). While many geophysical methods can locate and delineate fractures or faults and other mechanical discontinuities from microseismicity and time-lapse geophysical surveys, there is a need to extract physically measurable parameters that are directly linked to hydraulic and mechanical properties of fractures.

A mechanical discontinuity in rock, such as a fracture, is a quasi-planar structural feature that usually exhibits lower tensile and shear strength than the immediately adjacent rock. This reduction in strength arises from the fracture topology that results from two rough surfaces in contact forming a quasi-two-dimensional network of voids through which fluids flow, and a network of discrete points of contact that are connected to the rock matrix that control the mechanical deformation of the fracture. These two networks combine to provide a full description of fracture geometry for a single fracture and connect the hydraulic and mechanical response of a fracture (Pyrak-Nolte and Nolte, 2016). A long-term goal is to remotely monitor changes in this fracture geometry that, in turn, are linked to physical properties of a fracture. Achievement of this goal is difficult because fractures and other mechanical discontinuities occur on a range of length scales from $10^{-9}-10^{5}$ m, i.e. from microcracks that occur within and between grains that compose the rock matrix, to fractures and joints that span across a rock unit, to faults that extend over multiple geologic units. This requires not only a scale-dependent interpretation of geophysical measurements but also a scaling relationship between fluid flow and fracture stiffness that depends on the fracture geometry.

In this chapter, fracture specific stiffness is presented as the nexus that links the hydraulic, mechanical, and seismic properties of a fracture. The effects of fracture aperture distribution, chemical channelization, and immiscible fluid-controlled chemical erosion on fracture specific stiffness are examined. An overview of the relationship between fracture specific stiffness and fluid is provided. This is followed by a section on the seismic interpretation of fracture specific stiffness and how dynamic and static fracture stiffnesses are related. The conclusions address current and future needs.

Fracture Specific Stiffness

Fracture specific stiffness is often used to characterize a fracture or joint because it is intimately related to the condition or state of the fracture void geometry. A joint consists of two rough surfaces that, when subjected to stress, come into contact and deform the rock matrix and the asperities in contact, both of which affect the size and shapes of the voids through which fluid flows. This changing fracture topology plays a fundamental role in predicting joint closure, and affects the mechanical and hydraulic response of a joint (Brown, 1987; Brown and Scholz, 1985; Zimmerman et al., 1991; Petrovitch et al., 2013).

Fracture specific stiffness was introduced by Goodman (Goodman et al., 1968) as an effective parameter to capture and provide a quantitative value for complicated joint topology without performing a detailed analysis of the fracture geometry, such as measuring surface roughness, contact area, and aperture distributions (spatial and probabilistic). In this empirical approach, a fracture sample is subjected to loading normal to the fracture plane while displacements are made across the fracture and across an equal length of intact material. Joint closure is taken as the difference between these two measurements.

Theoretical and numerical studies on joint closure have determined that joint or fracture displacement is affected by the deformation of the asperities, deformation of the half spaces that represent the "walls" or "matrix" that contains the fracture, and asperity interactions (Hopkins, 1991). Fig. 14.1 illustrates the contribution to the displacement—stress relationship of the deformation of the matrix and asperities, and the asperity interaction based on a simple example
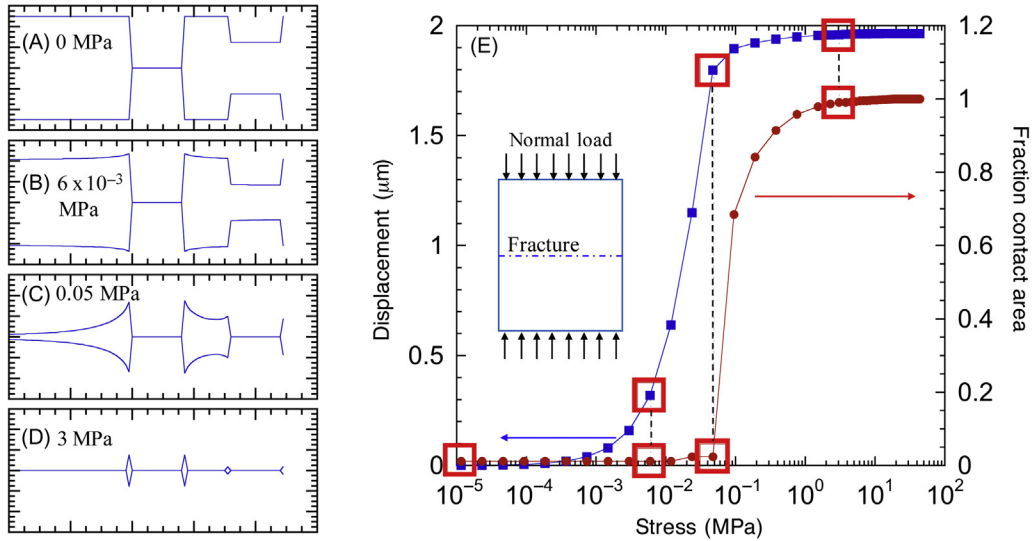
FIGURE 14.1 Deformation of a two asperity fracture (A) initially under no load, and then for stresses of (B) 0.006 MPa, (C) 0.05 MPa and (D) 3 MP. (E) Displacement (left *y*-axis) and contact area (right *y*-axis) as a function of stress illustrating the contribution to deformation from contact area, aperture, and matrix deformation.

from reference (Hopkins, 1991). In this example, the displacement−stress relationship is shown for two asperities under normal loading (i.e. loading normal to the fracture plane) with only one asperity initially in contact (Fig. 14.1A). The stress axis is given on a log scale to provide insight into the details of the displacement−stress curve (Fig. 14.1E). Fig. 14.1E also shows the change in contact area with increasing stress. As stress on the fracture increases (Fig. 14.1A and B), the initial asperity in contact shortens in length, making a small contribution to the deformation, and the matrix walls deform, affecting the void geometry and causing deformation of the second asperity. As the stress continues to increase (Fig. 14.1B and C), the deformation of the matrix dominates the displacement and there is very little change in contact area. Deformation of the matrix results in large apertures immediately adjacent to the asperities (Fig. 14.1C). After the second asperity comes into contact, the contact area initially increases rapidly with stress but the displacement begins to approach an asymptote. The asymptotic approach occurs because the few remaining high-aspect-ratio voids, that formed around the asperities, are difficult to close with increasing stress (Fig. 14.1D).

On probabilistic fracture aperture distributions, Hopkins (1991) showed numerically that deformation of the asperities under normal loading accounts for only 5%−10% of the total deformation of the fracture. The deformation of the half spaces (fracture walls or rock matrix) significantly affects the void volume, and asperity interactions affect when an asperity will come into contact with the other fracture surface. Thus, deformation of the void space, the increase in number of contacts, and the material properties of the asperities and rock affect fracture displacement and hence fracture specific stiffness.

As mentioned, fracture specific stiffness is determined from experimental measurements by taking the difference in displacement measured across the fracture relative to the displacement

measured across an equal length of an intact region. This difference is the excess displacement caused by the deformation of the voids and asperities. Fracture specific stiffness is determined from the inverse of the tangent slope of the fracture displacement−stress curve. Fig. 14.2 shows normal fracture specific stiffness as a function of stress, calculated from displacement measurements for single fractures in 13 different granitic samples for a range of specimen sizes (Pyrak-Nolte and Morris, 2000). From this laboratory data, it is observed that normal fracture specific stiffness changes nonlinearly with stress and tends to asymptote to a constant value at high stress, and fractures with larger dimensions tend to be more compliant (lower stiffness). The nonlinearity is attributed to the nonlinearity in the stress-fracture displacement curves that result from an increasing number of asperities coming into contact with increasing stress (Hopkins, 1991). The asymptotic approach to a constant stiffness at high stress occurs when the contact area is no longer changing with increasing stress, although significant void space may still exist that can accommodate the deformations (Cook, 1992). It should be noted that if additional significant stress were applied to a fracture, another inflection point would occur as the stiffness would continue to increase, and contributions from plastic deformation or other nonelastic behavior would need to be taken into account. The decrease in fracture specific stiffness with increasing fracture length arises from the probability that larger samples will maintain the presence of large apertures. For example, in Fig. 14.1A, if a core of this fracture was taken through only the void region on the left (Fig. 14.1A), there would be no asperities to maintain the aperture and the two fracture surfaces would be in contact, yielding a high normal fracture specific stiffness compared to that for the entire fracture (Morris, 2012).
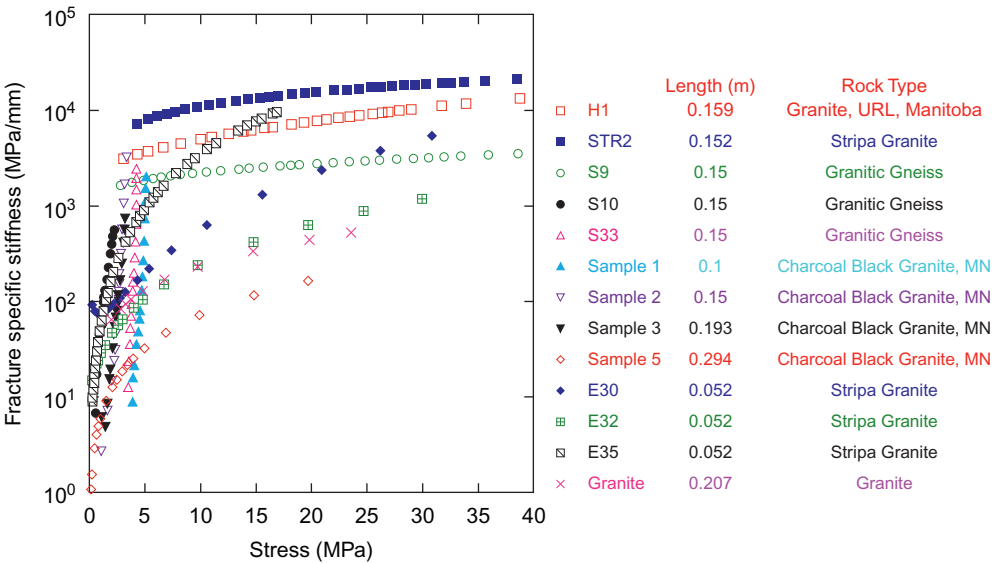

FIGURE 14.2　Fracture specific stiffness as function normal stress. *Source: From Morris, J.P., 2012. A numerical investigation of the scaling of fracture stiffness. Proceedings of the American Rock Mechanics Association Symposium, 24–27 June, Chicago, IL, USA.*

Fractures have shear fracture specific stiffness related to shear deformation of voids and changes in contacts caused by stresses parallel to the fracture plane. While normal fracture specific stiffness is easily measured in the laboratory using the approach described above, determination of shear fracture stiffness from displacement measurements is complicated by the need to define a length-scale for displacement measurements across the rock matrix and the fracture. An alternative method for estimating normal and shear stiffness in the laboratory or the field is based on the velocity and attenuation of transmitted/reflected seismic waves (Pyrak-Nolte et al., 1990b; Lubbe et al., 2008). (Details on this approach are given later in this chapter and the reader is also referred to Pyrak-Nolte et al., 1990b; Choi et al., 2014.) In the elastic regime, changes in normal and shear stiffness usually exhibit the same trends with changes in stress but differ in magnitude. For example, Fig. 14.3 shows the normal and shear stiffnesses (Pyrak-Nolte et al., 1990b) for a single fracture in quartz monzonite as a function of normal stress. Both values of stiffness increase with increasing stress up to 20 MPa and then appear to approach an asymptote. The changes in normal and shear stiffness are intimately linked through the deformed geometry of the fracture. The ratio of shear to normal stiffness depends on the loading conditions (uni-axial, bi-axial, or mixed-mode), the ratio of applied normal to shear stress, and the roughness of the fracture surfaces (Choi et al., 2014). This chapter focuses on the link among normal fracture specific stiffness, fluid flow, and seismic wave transmission.

In the subsurface, fractures will open and close in response to changes in stress, to changes in pressure and from alteration by geochemical processes. Very little experimental research has examined the effect of mineral precipitation on fracture geometry (Noiriel et al., 2011) or on fracture specific stiffness. However, substantial research has been performed on the effects of geochemical reactions/interactions on the geometry of fractures under ambient (Szymczak and Ladd, 2004) and stress conditions (Elkhoury et al., 2013; Ameli et al., 2014). During reactive flow, experiments have shown that the alteration of fracture surface roughness, contact area, and fracture apertures (i.e. void geometry) depends on reactive transport rates and local
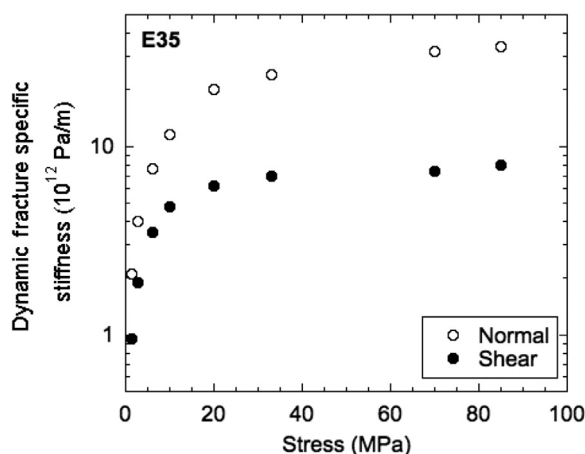

FIGURE 14.3   Normal and shear fracture specific stiffness as a function of normal stress from measurements of the transmission of compressional and shear waves across a single fracture. *Source: Based on data from Pyrak-Nolte, L.J., Myer, L.R., Cook, N.G.W., 1990b. Transmission of seismic waves across natural fractures. J. Geophys. Res. 95 (B6), 8617–8638.*

reaction rates for a fracture under no stress or under stress (Noiriel et al., 2011; Szymczak and Ladd, 2004; Elkhoury et al., 2013; Ameli et al., 2014). These studies have shown that chemical dissolution may or may not occur uniformly across a fracture resulting in a range of behaviors from homogenization of the flow path geometry to strong channelization.

Effect of Fracture Geometry on Fracture Properties

A Monte Carlo numerical study is presented that examines the effect of eroding different subsets of the fracture geometry through transport-dominated dissolution on fracture displacement. The role of fracture specific stiffness and fluid flow as a function of stress and the fracture length scale are also explored. Three cases are compared: (1) an isotropic spatially correlated aperture distribution (referred to as FIso); (2) single phase geochemical channelization where all apertures along the connected flow path were eroded proportionally to the flux through an aperture (referred to as FChan); and (3) channelization controlled by the spatial distribution of two immiscible fluids where only apertures below a certain size were subjected to dissolution in proportion to flux through the aperture (referred to as FIm).

Generation of Fracture Geometry

The fracture aperture realizations were generated using a stratified percolation method which is a combination of a hierarchical cascade with random percolation, and is described in (Pyrak-Nolte and Nolte, 2016; Petrovitch et al., 2013; Pyrak-Nolte and Morris, 2000; Nolte and Pyrak-Nolte, 1991, 1997). In this approach, the fracture aperture and contact area distributions are generated intrinsically rather than starting with two rough surfaces in contact. The degree of spatial correlation in the aperture distribution is controlled by the hierarchical cascade, and the probabilistic distribution of apertures is controlled by the random percolation component of the method.

For comparison with previous research (Pyrak-Nolte and Nolte, 2016), initially, 100 fracture aperture realizations (FIso) were generated on the largest scale, 512×512 array (or $1\,m \times 1\,m$). Then, 200, 400, 800, and 1600 subpatterns from each 512×512 pattern were randomly selected to create fractures with lengths of 0.5, 0.25, 0.125, and 0.0625 m, respectively. The number of subsections increased with decreasing fracture sampling length to ensure generation of representative statistics, and because fracture geometry varies significantly at the short length scales. On the smallest scale, a fracture can be almost entirely within a region of contact (white regions in Fig. 14.4) or regions of apertures. For example, the void area ranged between 0% and 98% over 1600 fracture samples with a length of 0.0625 m, while for fractures sampled on the 1-m scale, the void area only ranged between 48% and 71% for 100 realizations. The average void area for the 0.625- and 1-m fracture lengths were similar: 60% and 62%, respectively.

After generation of the FIso fractures, simulated chemical erosion was applied on the 1-m scale under no load, from which the small-scale regions of the fractures were randomly sampled. Channelized fractures (FChan) were created by allowing dissolution only in voids along the connected flow path. FChan simulates dissolution that might occur during transport-dominated single-phase flow (Fig. 14.4B). The flux is large in larger-aperture voids, leading to preferential erosion of the critical path which is the path of highest apertures (Pyrak-Nolte and
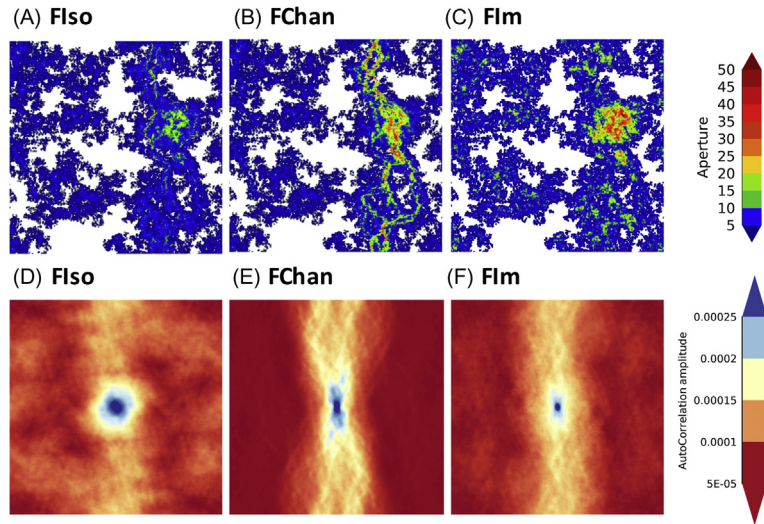
FIGURE 14.4 An example of 1 out of 100 fracture aperture distribution realizations (top row) and corresponding autocorrelation function (bottom row). Fracture aperture distribution and autocorrelation function for (A, D): FIso. an isotropic spatially correlated aperture distribution; (B, E): FChan, a channelized fracture with an anisotropic aperture distribution; and (C, F): FIm, a fracture eroded under immiscible transport conditions leading to a slight anisotropy in the flow paths.

Cook, 1988). For FIm (Fig. 14.4C), dissolution was simulated for the case when two immiscible fluids occupy a fracture, but only the wetting phase is chemically reactive. In this immiscible approach, the nonwetting nonreactive phase occupied the larger apertures in a fracture, thus restricting dissolution to only the smaller connected apertures through which a reactive wetting phase flowed. In other words, only the voids along the perimeter of the connected flow paths between the inlet and out of the sample experienced erosion.

Fracture Geometry, Fracture Displacement, and Fracture Stiffness

For each sample length scale and all fracture realizations (FIso, FChan, and FIm), fracture deformation as a function of stress was simulated using a combined conjugate-gradient method and fast-multipole method (Pyrak-Nolte and Morris, 2000; Petrovitch, 2013). Fluid flow, fluid velocity, and fluid pressures as a function of stress were determined from a flow network model (Petrovitch et al., 2013; Ameli et al., 2014; Cheng et al., 2004) applied to the deformed fractures. The readers are referred to the citations for additional details on the model.

Though the difference in fracture void geometry may appear small (Fig. 14.4), the alteration of selective subsets of the fracture geometry affects the deformation and hence fracture specific stiffness (Fig. 14.5). Fig. 14.5A shows the average fracture specific stiffness as a function of stress at the 1-m scale for the unaltered fracture (FIso) and the chemically eroded conditions, FChan and FIm. As stress increases, the average fracture specific stiffness increases as the voids deform, the contact area increases and the apertures in the fracture are reduced. The chemically eroded fractures on average are less stiff than the unaltered fracture (FIso) at all stresses.
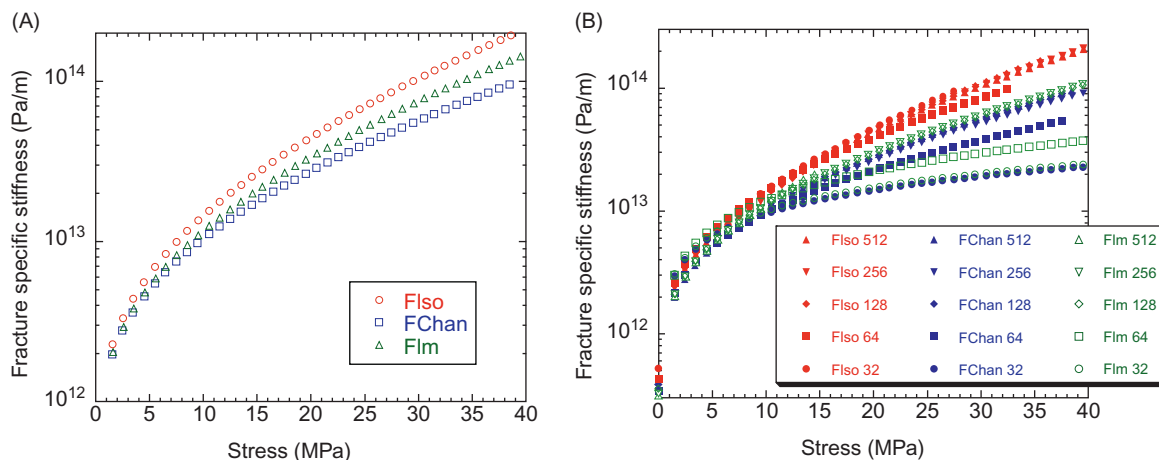
FIGURE 14.5 (A) Stiffness versus stiffness for the 1-m scale and (B) stiffness versus stress for different fracture length scales for FIso, FChan, and FIm.

Compared to the original FIso fractures, chemical erosion of the fracture leads to an increase in void volume of 27% and 18% for FChan and FIm, respectively, and produces more compliant fractures. Similarly, the average maximum displacement of the 1-m fractures increased from 2.85 μm for the unaltered pattern (FIso) to 3.68 and 3.32 μm for FChan and FIm, respectively. As shown by Pyrak-Nolte and Cook (1988) from a conservation of volume approach, and by Hopkins (1991) from numerical modeling, fracture deformation in the elastic regime is dominated by deformation of the voids.

Preferentially eroding the dominant flow path (FChan) or the connected path of smallest apertures (FIso) affects the scale dependence of fracture specific stiffness compared to the FIso fractures. Fig. 14.5B provides a comparison of average fracture specific stiffness for FIso, FChan, and FIm for fracture length scales from 0.0625 to 1 m. When the spatial correlation of the fracture aperture distribution is isotropic, as for the uneroded fracture FIso, the average fracture stiffness is nearly scale-independent with small-scale fractures exhibiting slightly higher stiffnesses than longer fractures as observed in Morris (2012). However, selective erosion of subsets of the fracture voids leads to a dependence of average stiffness on fracture length and stress. A cross-over in the scale-dependence of stiffness with stress occurs near a stress of 10 MPa when the average void area of the fractures is roughly 30%. When the stress is less than 10 MPa, short fractures exhibit a slightly higher average fracture stiffness than longer fractures for FChan and FIm, similar to FIso fractures. However, for stresses greater than 10 MPa, the scale dependence on stiffness is reversed for FChan and FIm, i.e. longer fractures are stiffer than shorter fractures. The cross-over behavior of stiffness with scale has only been observed for aperture distributions with persistent channels (Pyrak-Nolte and Nolte, 2016).

This study shows that fracture specific stiffness is sensitive to the void volume of a fracture as well as to the spatial distribution of the void volume. Pyrak-Nolte and Nolte (2016) examined the stiffness of fractures with the same void volume but with different contact area. For the same void volume, fractures with more contact were more compliant because the apertures were larger than for those with less contact area. Thus fracture stiffness is an effective

parameter that captures the changes in both apertures and contact area that occurs as a fracture is opened/closed from physical and geochemical processes. These geometrical alterations to a fracture also affect fluid flow through a fracture and form the link between fluid flow and fracture specific stiffness.

Link Between Fracture Specific Stiffness and Fluid Flow

Many studies have been performed (and are ongoing) that examine the effect of fracture geometry on fluid flow through a fracture. These studies have shown that fracture geometry is complex and sensitive to even slight alterations, but also that volumetric flow rates through a fracture ultimately depend on the size and spatial distribution of apertures and contact area (Berkowitz, 2002; Jaeger et al., 2007; Lang et al., 2015). In 2013, Petrovitch et al. (2013) demonstrated numerically that fracture specific stiffness can be used as an effective parameter to capture the complicated deformed geometry of a fracture. More importantly, they showed that stiffness can provide the basis of a scaling relationship for fluid flow through fractures. This was an important development because fracture specific stiffness can be estimated from seismic wave attenuation and velocity (Majer et al., 1988).

Petrovitch et al. (2013) performed an analysis of fracture deformation and fluid flow through fractures as a function of scale (fracture length) for isotropic random distributions of weakly correlated apertures. Their work showed that a flow-stiffness scaling relationship existed that exhibited two regimes: an effective medium regime where fluid flow is dominated by the void volume or porosity of a fracture, and a percolation regime where fluid flow is dominated by the connectivity of the flow paths through a fracture. This relationship was possible to define because fracture specific stiffness was found to be a surrogate for void area that is traditionally used in percolation studies. The Petrovitch critical scaling relation is based on finite-size scaling effects in percolation theory and is given by

$$q\frac{L}{a_o^3} = L^{-t/\mu}F\Big[(\kappa - \kappa_c)L^{1/\mu}\Big] \tag{14.1}$$

where q is the volumetric flow rate, L is the scaled length of the fracture ($L = L'/L_o$ where L' is a particular scale and L_o is the largest scale), a_o is the mean aperture at the largest scale, κ is the fracture specific stiffness, κ_c is the critical fracture specific stiffness, t/μ is the flow exponent, and μ is the geometric correlation exponent ($\mu = 4/3$).

In 2016, Pyrak-Nolte and Nolte (2016) demonstrated that Petrovitch's flow-stiffness relationship given by Eq. (14.1) did not collapse the flow-stiffness data for highly-channelized fractures such as FChan. They extended Eq. (14.1) to enable application to a wide range of fractures with weak and strong spatial correlations, as well as chemically eroded fractures, by including the effect of spatial correlations in the aperture distribution, and accounting for changes in void volume and the critical neck (the smallest aperture along the critical path; Pyrak-Nolte and Cook, 1988). Their extended scaling relationship is

$$q\frac{L}{a_0^3} = (L\alpha)^{-t/\mu}F\Big[(\kappa - \kappa_c)(L\alpha)^{1/\mu}\Big] \tag{14.2}$$

where α is the ratio of the correlation exponent at a stress to the correlation exponent at the lowest stress at the largest scale. The flow q is scaled by a_0^3 which is the ratio of the average mean aperture at the largest scale to the average aperture of the critical neck at the largest scale. The threshold parameter κ_c is the critical stiffness at the critical threshold and is determined by extrapolating the stiffness at the critical area to infinite size. They observed that for all fracture conditions, except highly eroded channelized fractures, that κ_c is independent of scale. Even when a fracture is highly channelized, a scale-dependent κ_c continues to enable data collapse, as smaller subsections of the highly channelized fractures require more stress to close the critical path than at larger scales.

Anisotropic Flow Paths in a Fracture

One issue not addressed in these previous studies is the treatment of fractures that exhibit anisotropic flow. For the fracture realizations FChan and FIm, fluid flow through the fractures was simulated for two orientations, parallel and perpendicular to the flow direction used to simulate chemical erosion (in the vertical and horizontal direction, respectively, in Fig. 14.4). As shown in the autocorrelation functions in Fig. 14.4E, FChan exhibits strong anisotropy in the spatial aperture distribution because of the highly eroded dominant path. The anisotropy in the spatial correlation is much less for FIm but still contains longer spatial correlation lengths in the vertical direction, i.e. the dominant direction of chemical dissolution in the fracture. The original pattern, FIso, has an isotropic autocorrelation function. The effects of isotropic and anisotropic spatial correlations on average permeability from 100 patterns of FIso, FChan, and FIm are shown in Fig. 14.6. The spatially isotropic aperture distributions of the FIso patterns results in the very similar values of average permeability (Fig. 14.6) for the two orthogonal flow directions. The chemically eroded fractures, FChan and FIm, yield anisotropic average permeability that differ in magnitude for flow taken parallel and perpendicular to the eroded channels in the
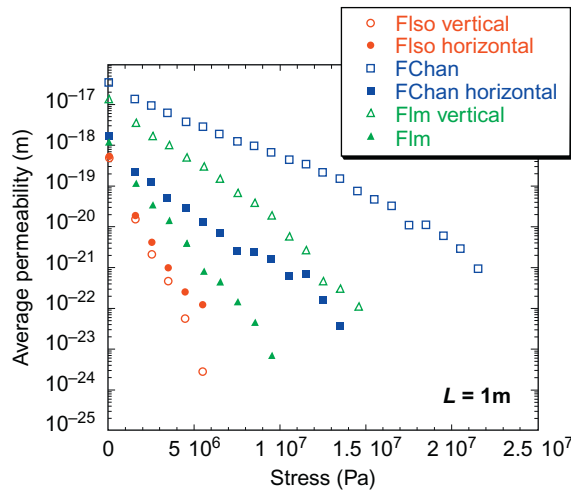

FIGURE 14.6 Average permeability as a function of stress for fractures FIso, FChan, and FIm for a fracture length = 1 m for both parallel (vertical) and perpendicular (horizontal) to the flow direction during chemical erosion.

fracture. Flow is more persistent at high stresses for flow simulations performed parallel to the eroded channels. The rate at which flow decreases with increasing stress also varies between FIm and FChan.

A key issue is how this anisotropy in average permeability affects the flow−stiffness relationship. For both FIm and FChan, there is only one value of average normal stiffness at each stress but the flow is significantly different in the two directions. In both Eqs. (14.1) and (14.2), the parameters that are the same for both orientations of flow are the average normal stiffness as a function of stress, κ, and the mean aperture of the fracture. Using the Petrovitch scaling approach, the flow−stiffness data do not collapse to a single curve (Fig. 14.7A) and the anisotropic flow is apparent even for the FIso fractures. Mean aperture is not a sufficient characterization of a fracture in terms of fluid flow.

Pyrak-Note and Nolte had extended Eq. (14.1) to account for spatial correlations in the aperture distribution and incorporated the aperture of the critical neck. However, they did not consider the effect of anisotropic flow that arises from physical and chemical processes that preferentially and directionally alter subsets of the fracture geometry. In the presence of anisotropic flow, the critical neck in Eq. (14.2) differs for the two orthogonal flow directions because the critical path is different (e.g., Fig. 14.4). The differences in the critical path are not significant for the unaltered fractures FIso where the critical neck varies by $\sim 1.5\,\mu m$ (Table 14.1) though significant enough to affect the collapse using Eq. (14.1) that only uses mean aperture.
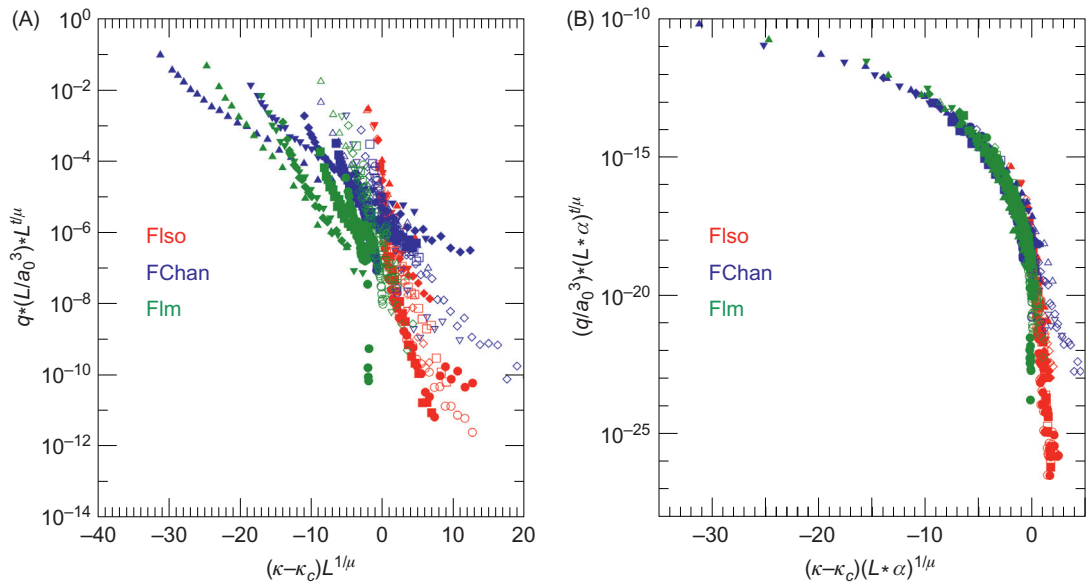
FIGURE 14.7 (A) Flow−stiffness relationship based on Petrovitch scaling from Eq. (14.1). (B) Flow−stiffness relationship based on Pyrak-Nolte and Nolte extended scaling from Eq. (14.2), for unaltered (FIso, red) and chemically eroded fractures (FIm, green; FChan, blue) as a function of scale for vertical (filled symbols) and horizontal (open symbols) flow directions. The shape of the symbol indicates the fracture length scale: 0.0625 (circles ●), 0.125 (squares ■), 0.25 (diamonds ◆), 0.5 (filled inverted triangle ▼), and 1 m (filled triangle ▲). Scaled flow has units of m³/s and scaled fracture.

TABLE 14.1 Aperture of the Critical Neck, a_c, Flow Exponent, t/μ, Critical Void Area, A_c, and Critical Stiffness, κ_c, as a Function of Fracture Length for Fracture Simulations FIso, FChan, and FIm

Fracture name	Flow direction	a_c (μm)	t/μ	A_c	0.0625 mκ_c (TPa/m)	0.125 mκ_c (TPa/m)	0.25 mκ_c (TPa/m)	0.5 mκ_c (TPa/m)	1 mκ_c (TPa/m)
FIso	Vertical	5.38	2.8474	0.56	2.39	2.39	2.39	2.39	2.39
	Horizontal	6.96	2.7321	0.55	2.61	2.61	2.61	2.61	2.61
FChan	Vertical	87.3	2.7406	0.17	31.5	42.5	55.0	55.0	60.0
	Horizontal	25.0	2.315	0.49	9	12	16	26	42
FIm	Vertical	72.1	2.6858	0.30	24	29	40	42	42
	Horizontal	17.7	2.2183	0.51	9	10	14	18	22

However, for FIm and FChan the critical paths differ significantly with critical necks that are 4 and 3.5 times larger, respectively, in the the direction of the chemical erosion than in the orthogonal (horizontal) direction. From percolation studies, macroscopic conductivity is dominated by the critical neck for a network of strongly inhomogeneous conductances (Ambegaokar et al., 1971; Pollak, 1972). For percolation in anisotropic fracture aperture distributions, this results in directionally dependent average permeability and the ratio of the spatial correlation exponents, α, as a function of stress.

The transport exponent, t/μ, and critical stiffness, κ_c, also differ for anisotropic aperture distributions because both are based on the critical void area fraction, A_c, i.e. the area at which a percolation system, in the infinite limit, will be connected and support flow. As shown in Table 14.1, the isotropic nature of FIso fractures is apparent because A_c is nearly the same for the two directions. When chemical dissolution occurs along the critical path, as in FChan, the critical area fraction is very low ~ 0.17. When only the smallest apertures along the critical path are eroded, as in FIm, an area fraction of at least 0.3 is needed, on average, to support flow in the direction parallel to the erosion. These values are much lower than for the unaltered fracture, FIso, or for flow in the direction perpendicular to the chemically induced channels, where A_c is $\sim 0.50-0.55$.

By using directionally dependent transport exponents, critical necks and spatial correlation exponents in Eq. (14.2), all these data collapse to a single curve (Fig. 14.7B) for FIso, FChan, and FIm. This striking universal collapse suggests that the fundamental basis of hydromechanical coupling in a fracture is the deformable void volume which affects both the connectivity of flow paths through a fracture and the fracture specific stiffness.

The functional form of the flow−stiffness relationship is the same as that found by Petrovitch et al. (2013) for weakly correlated random aperture distributions and by Pyrak-Nolte and Nolte (2016) for spatially correlated aperture distributions. As both of these studies have described, the flow−stiffness relationship has two regimes: an effective medium region $\{(\kappa - \kappa_c)(\alpha L)^{1/\mu} < -1.0\}$, where the permeability is dominated by the porosity of the fracture; and a critical percolation regime $\{(\kappa - \kappa_c)(\alpha L)^{1/\mu} \approx 0.0\}$, where permeability is controlled by the connectivity of the flow paths. The effective-medium regime applies to large-scale fractures where fluid flow is in the direction of large-aperture channels such as those induced by chemical erosion in FChan, or in the direction of enhanced critical necks from chemical erosion such as in FIm.

Small-scale fractures may contain only one flow path whose connectivity is critically affected by small changes in stress even in fractures with chemically enhanced critical paths. An important part of the curve occurs near $(\kappa - \kappa_c)(\alpha L)^{1/\mu} \sim -1.0$ which is the transition between the effective medium regime and percolation regime. Fractures that fall into this region of the curve exhibit flow behavior that has contributions from both aperture (or fracture porosity) and flow path connectivity that play competing or supportive roles in the maintenance of flow. In this crossover regime, the flow path geometry and velocity field transitions from relatively homogeneous flow paths to filamentary paths dominated by the critical path (Petrovitch et al., 2013; Pyrak-Nolte and Cook, 1988).

The flow−stiffness relationship was obtained from averages of flow and stiffness at each scale from a Monte Carlo study that performed analysis of data from 9300 fracture realizations. Most laboratory and field studies do not have access to sufficient samples or measurements to achieve an average response. Therefore, an empirical fit to the flow−stiffness relationship is provided to enable other studies to compare measurements to the flow stiffness relations. The empirical fit is shown in Fig. 14.8 and is given by

$$q_{scaled} = exp\left(\frac{-\beta}{|\kappa_{scaled} - 1.5|^{0.22}}\right) \tag{14.3}$$

where q_{scaled} is $q(L/a_o^3)(L\alpha)^{t/\mu}$, κ_{scaled} is $(\kappa - \kappa_c)(L\alpha)^{-1/\mu}$, and β is an arbitrary factor (in this case ~ 51).

The collective data collapse provided by Eq. (14.2) for a wide range of fracture topologies in this and from previous studies strongly supports this scaling relationship between fluid flow and fracture specific stiffness for the case of laminar flow. Fracture specific stiffness is intimately linked to the mechanical deformation of the fracture void volume which in turn controls fluid flow through a fracture. As will be shown in the next section, fracture specific stiffness can be interpreted from measurements of elastic wave velocity, and transmission and reflection coefficients. The link between fluid flow and fracture specific stiffness is key to the development of remote monitoring systems for characterizing the hydraulic integrity of caprocks and other subsurface barriers.
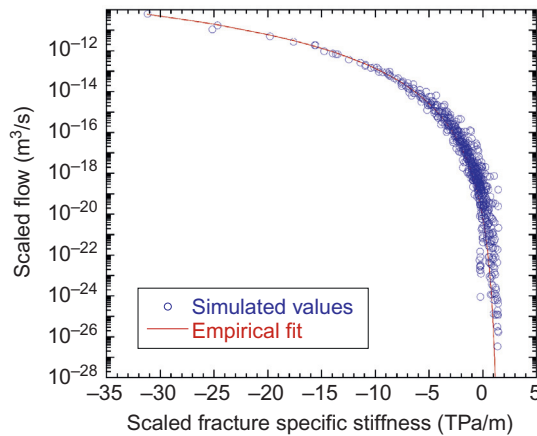

FIGURE 14.8 Empirical fit from Eq. (14.3) to the flow−stiffness relationship. Stiffness has units of TPa/m.

Interpreting Fracture Stiffness From Seismic Waves

A current goal that cuts across many subsurface engineering activities such as fluid sequestration, geothermal energy development, and oil and gas production, is the desire for adaptive control of subsurface fractures (Pyrak-Nolte and DePaolo, 2015). The ability to remotely monitor changes in fractures at any scale requires a link between the macroscopic scattered wave-field and a property of a fracture that is linked to fluid flow. As presented in the previous section, fracture specific stiffness, κ, is an effective parameter that captures the complexity of a deformed fracture in a single parameter and forms the basis of a scaling relationship with fluid flow. The flow−stiffness relationship presented in the previous section was based on static fracture specific stiffness, κ_{static}, which is determined from measurements of mechanical deformation of a fracture. On the other hand, many studies have shown that dynamic fracture specific stiffness, $\kappa_{dynamic}$, can be estimated from compressional and shear waves propagated through fractured media (Pyrak-Nolte et al., 1990b; Lubbe et al., 2008; Choi et al., 2014; Majer et al., 1988; Hedayat et al., 2014). Compressional and shear waves produce local changes in stress and strain as these waves propagate through a medium. As a wave propagates across a fracture, energy is partitioned between transmitted and reflected waves that are related by a discontinuity in displacement that is inversely proportional to dynamic fracture specific stiffness (Cook, 1992). An important question is whether $\kappa_{dynamic}$ is connected to κ_{static}, and whether $\kappa_{dynamic}$ could be used in the flow−stiffness relationship.

Pyrak-Nolte et al. (1990b) measured κ_{static}, and $\kappa_{dynamic}$ as a function of normal stress for three samples of quartz monzonite rock, each of which contained a single throughgoing fracture (Fig. 14.9). $\kappa_{dynamic}$ and κ_{static} exhibited the same trends with stress (Fig. 14.9A). At every stress for all three samples, $\kappa_{dynamic} > \kappa_{static}$ (Fig. 14.9B). The discrepancy between $\kappa_{dynamic}$ and κ_{static} has been attributed to frictional effects similar to the difference between dynamic and static elastic moduli of rock (Pyrak-Nolte et al., 1990b), as well as the distributions of fracture specific
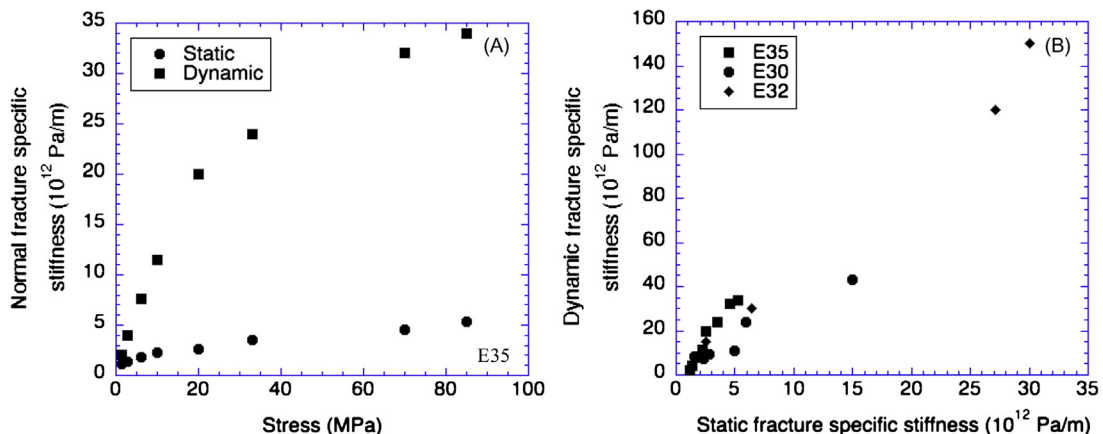

FIGURE 14.9   (A) Comparison of static and dynamic normal fracture specific stiffness based on data for sample E35 from Pyrak-Nolte et al. (1990b). (B) Dynamic versus static normal fracture specific stiffness for three different samples each containing a single fracture Pyrak-Nolte et al. (1990b).
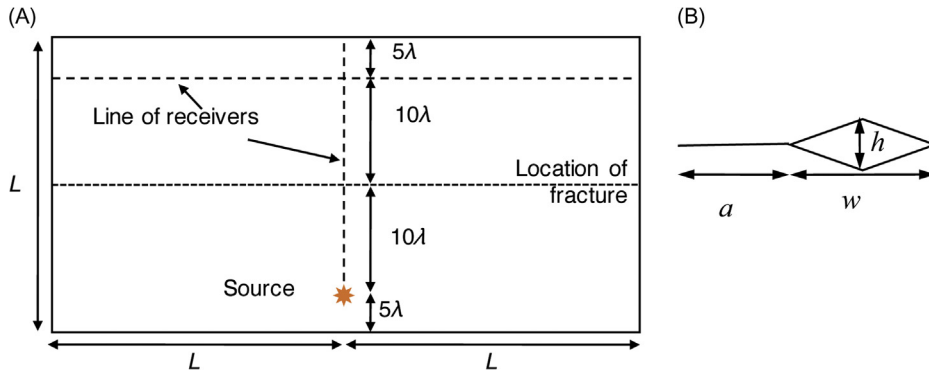
FIGURE 14.10   (A) Computational domain for simulation for a single fracture composed of N unit cells (see Table 14.2). (B) Unit cell where a is the contact length, w is the void width, and h is the height of the void.

stiffness within a fracture (Pyrak-Nolte and Nolte, 1992; Acosta-Colon et al., 2009). The interpretation of $\kappa_{dynamic}$ depends on the amount of contact/void region under a seismic probe and on whether energy is scattered out of the collection area of the probe.

A heuristic study was performed to determine if the difference in $\kappa_{dynamic}$ and κ_{static} occurs for even simple periodic fracture geometries (Fig. 14.10 and Table 14.2). A 2-D Discontinuous Galerkin method was used to simulate compressional wave propagation across fractures having a range of simple void geometries. The displacement discontinuity method (Pyrak-Nolte et al., 1990b; Choi et al., 2014; Pyrak-Nolte et al., 2016) was used to analyze the numerical results to estimate dynamic fracture specific stiffness and to determine the sensitivity of the stiffness to fracture void geometry. These same fractures were then deformed using the same mechanical deformation code as in the flow-stiffness study to enable the comparison of static, κ_{static}, and dynamic, $\kappa_{dynamic}$, fracture specific stiffnesses.

Simulation of Compressional Wave Transmission

A discontinuous Galerkin (DG) method was used to simulate compressional wave propagation in two-dimensions across a single fracture that was represented by an array of microcracks. The DG method provides highly accurate solutions for waves to travel over multiple wavelengths with minimal dispersion (Dumbser and Käser, 2006). DG has been used to incorporate displacement discontinuity representations of finite-size fractures (De Basabe et al., 2011) or explicitly to model the physical geometry of the fracture (Petrovitch, 2013; Shao et al., 2015; Ye et al., 2016). Information about the DG method used in this study can be found in the references (Petrovitch, 2013; Shao et al., 2015; Ye et al., 2016). In this study, elastic wave interaction with geometry of the fracture is explicitly modeled using DG to explore the link between fracture specific stiffness interpreted from elastic wave transmission.

The simulation domain (Fig. 14.10A) is defined as an isotropic medium (compressional wave velocity $V_p = 3600$ m/s, a shear wave velocity $V_s = 1900$ m/s, density $\rho = 2080$ kg/m^3) with a single fracture centered in the domain. The height of the domain is $L = 0.108$ which is 30 times the central wavelength ($\lambda_c = 3.6$ mm at 1 MHz) and the length of the domain is $2L$. The

TABLE 14.2   Contact Length, a, Void Width, w, Asperity Spacing $(a + w)$, Number of Unit Cells, κ_{static} and $\kappa_{dynamic}$ for Different Fracture Simulations

Fracture simulation number	a (mm)	w (mm)	$a + w$ (mm)	Number of unit cells	$\kappa_{dynamic}$ (TPa/m)	κ_{static} (TPa/m)
F1	0.1	1	1.1	981	4.64	6.30
F2	0.5	1	1.5	720	9.14	11.1
F3	1	1	2	540	15.3	16.0
F4	2	1	3	360	35.5	24.4
F7	1	0.01	1.01	1069	132	∞
F8	1	0.05	1.05	1028	122	∞
F9	1	0.1	1.1	981	118	189
F10	1	0.3	1.3	830	67.2	92.6
F11	1	0.5	1.5	720	36.5	44.2
F12	1	2	3	360	7.54	5.74
F13	0.2	0.9	1.1	981	6.66	9.15
F14	0.4	0.7	1.1	981	13.9	17.8
F15	0.6	0.5	1.1	981	27.5	35.6
F16	0.8	0.3	1.1	981	58.8	80.9
F17	0.3	0.3	0.6	1800	38.6	48.6
F23	0.6	0.3	0.9	1200	52.8	70.7
F24	0.4	0.3	0.7	1542	42.1	57.3
F25	0.2	0.3	0.5	2160	32.5	42.0

computational domain was designed to minimize interference from boundary reflections in signals propagated at normal incidence to the fracture, and to receive signals in the far-field. A broadband compressional wave point source was placed $10\lambda_c$ below the fracture with a line of virtual receivers that spanned the width of the domain $(2 L)$ located $10\lambda_c$ above the fracture. A second line of virtual receivers was located along a vertical line centered on the source. The receivers were spaced $0.5\lambda_c = 1.8$ mm apart in each line of receivers. A second computational domain with the same dimensions and physical properties, but with no fracture, was used to obtain an "intact" signal to use as a reference signal.

A colinear array of microcracks is used to simulate a fracture. The unit cell that represents a microcrack is defined by the contact length, a, the void width, w, and the void height, h (Fig. 14.10A). Simulations were performed for 18 fractures with different unit cell dimensions to determine the sensitivity of elastic waves to the details of the fracture void geometry. The values of a and w are given in Table 14.2 along with the number of unit cells that composed each fracture of length L. For these simulations, h was held constant at a value of 0.1 mm. The asperity spacing is also listed in Table 14.2 and is given by $(a + w)$, ranging from 0.5 to 3.0 mm.

Previous research has found that the displacement discontinuity theory captures scattering from a fracture composed of an array of microcracks similar to that based on a full scattering solution, but noted that deviations can occur when the wavelength is less than four times the microcrackspacing and also when the wavelength is of the same order as the void width (Angel and Achenbach, 1985; Myer, 2000).

Dynamic Versus Static Fracture Specific Stiffness

As noted in an earlier section, κ_{static} is sensitive to the void volume of a fracture as fractures with smaller volumes have larger κ_{static}. For the dynamic study, the effect of decreasing void volume was studied by maintaining the asperity spacing to ensure that observed changes were caused by a reduction in void volume and not changes in spacing (i.e. the number of unit cells was held constant). As the void volume decreased (Fig. 14.11A), the transmitted compressional wave increases in amplitude, decreases in arrival time, and increases in frequency. Fractures with large void volumes (signals from F1 and F13) resulted in more energy partitioning into reflected-modes than into transmitted-modes (Pyrak-Nolte et al., 1990b). As the contact area increases (or as the void width decreases) more energy is transmitted through the increased contact area. When $w < 0.1(a + w)$ or $\sim 0.03\lambda_c$, the fracture transmits almost as well as the intact domain (signal for F9 in Fig. 14.11A).

The dynamic stiffness, $\kappa_{dynamic}$ can be interpreted from compressional and shear waves propagated across a fracture (Pyrak-Nolte et al., 1990b; Lubbe et al., 2008; Choi et al., 2014; Majer et al., 1988). Transmission, reflection, and/or time delays from experimental measurements are used with the displacement discontinuity theory (Schoenberg, 1980; Pyrak-Nolte et al., 1990a; Caricione and Picotti, 2012) to estimate fracture specific stiffness. In this approach the
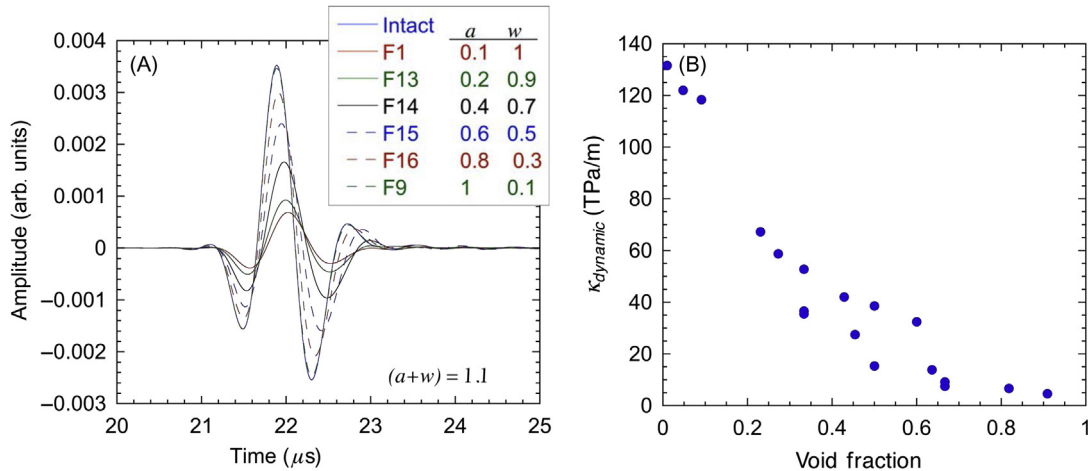

FIGURE 14.11   Simulated compressional waves transmitted across an intact sample and fracture samples with (A) the same asperity spacing ($a + w = 1.1$) but different contact length, a, and void width, w (a and w are in mm, central wavelength $\lambda_c = 3.6$ mm at 1 MHz). (B) Dynamic fracture specific stiffness from simulated waves as a function of the ratio of void width to asperity spacing.

discreteness of the fracture is maintained such that waves are not delayed nor attenuated until crossing the fracture. This is a purely elastic representation, but it yields frequency-dependent group time delays, transmission and reflection coefficients, and produces energy partitioning of waves into body waves as well as guided modes that depend on fracture specific stiffness (Pyrak-Nolte et al., 2016; Shao et al., 2015).

To interpret fracture specific stiffness for each simulated fracture, a Fast Fourier Transform (FFT) of the intact signal is convolved with the complex conjugate of the transmission coefficient of displacement discontinuity theory (Pyrak-Nolte et al., 1990b; Choi et al., 2014). An inverse FFT of this product yields a "predicted" signal to compare to the signals from the fracture simulations. The stiffness that produces the lowest chi-squared value between the theoretical signal and a fracture signal is selected as $\kappa_{dynamic}$.

Values for $\kappa_{dynamic}$ as a function of fraction of voids ($w/(a+w)$) are shown in Fig. 14.11B. As was the case for κ_{static} in the earlier sections, $\kappa_{dynamic}$ decreases as the void volume increases. This suggests that similar to κ_{static}, $\kappa_{dynamic}$ is sensitive to the state (open, partially closed) of the fracture void geometry. Previous laboratory research on wave propagation across synthetic fractures with known contact area, and on natural fractures subjected to normal loading have also shown that elastic wave amplitudes, arrival times, and spectral content depend on the probabilistic and spatial distributions of contact area and voids (Cook, 1992; Majer et al., 1988; Acosta-Colon et al., 2009; Kendall and Tabor, 1971; Oliger et al., 2003).

A comparison of $\kappa_{dynamic}$ and κ_{static} shows a nearly proportional relationship between these two different properties (Fig. 14.12). The values for κ_{static} were determined by simulating fracture displacement as stress was applied to the fracture, and then taking the slope of the stress—displacement curve. The two properties $\kappa_{dynamic}$ and κ_{static} are not equal but do share a similar trend. Whether $\kappa_{dynamic}$ is less, greater or equal to κ_{static} depends on the method for estimating $\kappa_{dynamic}$ from the elastic wave data. For instance, applying the full wave form fit described above yields $\kappa_{dynamic} < \kappa_{static}$ with the data points falling above the $x = y$ line.
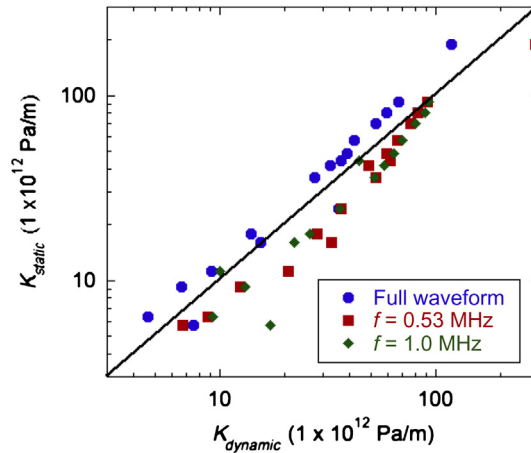

FIGURE 14.12 Comparison of $\kappa_{dynamic}$ and κ_{static} based on a full-waveform interpretation, and for frequencies of 0.53 and 1.0 MHz. The $y = x$ line is shown for comparison.

An alternate approach to extract the dynamic fracture stiffness is to use the analytic solution for wave transmission at normal incidence at a single frequency, namely,

$$T = \frac{1}{1 - \frac{i\omega Z}{2\kappa}} \qquad (14.4)$$

where $\omega = 2\pi f$ is the angular frequency (and f is the frequency of the signal), Z is the seismic impedance of the matrix containing the fracture (Z = density * phase velocity in the matrix) and $\kappa = \kappa_{dynamic}$. The transmission coefficient, T, at a specific f can be determined from the ratio of the Fourier spectrum of the signal from the fracture simulation to the Fourier spectrum from the signal from the intact simulation. Taking the absolute value of Eq. (14.4) and rearranging, yields

$$\kappa = \frac{\omega Z}{2\sqrt{\frac{1}{T^2} - 1}} \qquad (14.5)$$

which can be solved directly for $\kappa_{dynamic}$. Eq. (14.5) was used to determine $\kappa_{dynamic}$ for frequencies of 0.53 and 1 MHz as shown in Fig. 14.12. At these particular frequencies, $\kappa_{dynamic} > \kappa_{static}$, but the trend is again the same. This confirms that $\kappa_{dynamic}$ and κ_{static} are closely connected, and that $\kappa_{dynamic}$ can be used as a surrogate for κ_{static}, and, more importantly, that $\kappa_{dynamic}$ can be used to interpret changes in fracture geometry and flow using remote geophysical methods.

SUMMARY

Applications of Findings to Carbon Storage

Caprock integrity is an important factor for the safe storage of CO_2 in the subsurface using structural trapping. The presence of natural fractures, faults, and other mechanical discontinuities pose the largest risk for the escape of stored CO_2 over long periods of time because these discontinuities are usually more permeable and more compliant than the host rock. In addition, changes in stress and pore pressure during and after injection can lead to the opening/closing of fractures, shear reactivation of preexisting mechanical discontinuities and initiation of new fractures. These geomechanical perturbations cause fundamental changes in fracture geometry that affect permeability and can create new pathways for CO_2 migration and chemical alteration of fractures as well as the rock matrix (Verdon et al., 2013; Bond et al., 2013).

Given the range of length scales for mechanical discontinuities in subsurface reservoirs, a key question when simulating long-term CO_2 storage scenarios (Rutqvist and Tsang, 2002) is how to upscale or include the physical response of fractures at scales smaller than the simulation cell size. The extended flow—stiffness relationship developed by Pyrak-Nolte and Nolte (2016), and shown here to apply to anisotropic fracture flow paths, provides insight, and a functional form (Eq. (14.3)) as an appropriate method for incorporating changes in the hydraulic behavior of fractures with different scales. This method is applicable to fracture alterations caused by changes in stress or pore pressure, and/or from geochemical reactions that result in channelized flow paths or nonuniformly eroded aperture distributions.

For example, stress in the subsurface increases with depth and changes with tectonic setting. The fluid flow response from similar fractures residing at different depths would vary because high stress at depth reduces fracture apertures and increases contact area. A simple cubic law approximation (Witherspoon et al., 1980) for fracture flow may capture the difference in flow between a shallow and deep fracture predicting that deep fractures support less flow because of reduced aperture caused by high stress. However, a cubic law approximation cannot capture changes in flow rate attributed to changes in flow path connectivity. Using the flow−stiffness relationship in a simulation, fractures at greater depth could be treated in the percolation regime, exhibiting dramatic changes in flow rate that can occur even for small changes in stress, while shallow fractures could be treated with an effective medium approach (Pyrak-Nolte and Nolte, 2016) with flow dominated by the porosity or volume of the fracture void space. These differences affect the outcome of simulation scenarios that examine changes in flow rate during and post injection of CO_2 as stresses and pressures equilibrate over time throughout a subsurface reservoir.

While the flow−stiffness relationship was developed for single fractures, the same concepts of effective medium and percolation regimes apply to sets of fractures and fracture networks. Connectivity-dominated flow paths through a fracture network will exhibit a rapid decrease in flow rate with increasing stress, and conversely a fracture system with multiple flow paths or highly channelized stress-resistance pathways will tend to support flow that decreases less rapidly with stress.

Application of this hydro-mechanical scaling and remote elastic wave characterization of fractured rock to subsurface carbon storage must also consider the range of length scales of mechanical discontinuities (i.e. microcracks, fractures, joints, and faults) at subsurface sites and the wavelength of the signal used to probe the rock. For example, an important question is how well the flow−stiffness relationship will scale from laboratory-based measurements, made on retrieved core samples, to borehole and cross-hole scales. This will depend on the ability to interpret fracture specific stiffness from the scattered wave field. Worthington (2007) made a compilation of values of fracture compliance obtained from compressional and shear wave data for scales spanning from the laboratory to the fault scale. These data are presented in Fig. 14.13A in terms of fracture specific stiffness. From this data set, fracture specific stiffness is observed to decrease with increasing fracture length from ∼0.05 to 100 m. However, interpretation of these data must take into account that the data were collected using frequencies that ranged from 1 MHz on the laboratory scale, to 20 kHz for the borehole scale, to 16−30 kHz for the crosshole scale, and to 140 Hz for the fault scale, for wavelengths ($\lambda = v/f$ where v is velocity and f is the frequency of the signal) of the order of millimeters to tens of meters, respectively.

The displacement discontinuity theory clarifies this observed trend in fracture stiffness with fracture length and wavelength. The displacement discontinuity theory has a built-in scaling parameter (Pyrak-Nolte et al., 2016) referred to as a characteristic frequency $\omega_c = \kappa/Z$. This characteristic frequency determines the range of facture specific stiffnesses that can be detected for a given frequency and given seismic impedance of the rock matrix based on the time delay (or velocity) and/or the reflection/transmission coefficients. For example, the wave speeds for compressional and shear body waves transmitted across a fracture are shown in Fig. 14.13B along with wave speeds for fracture interface waves, intersection waves, and coupled wedge waves. The wave speeds are normalized by the shear wave speed in the matrix and are shown as a
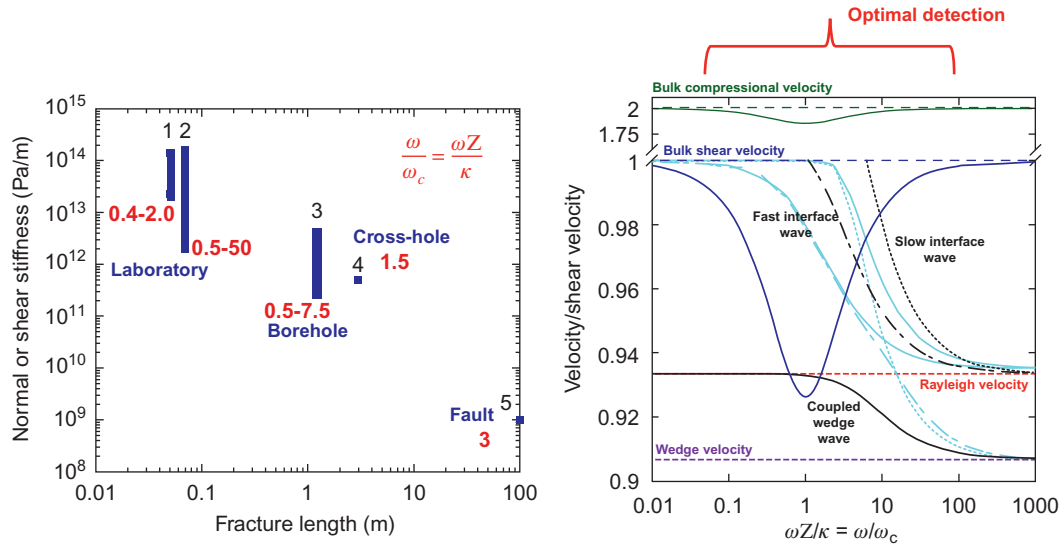
FIGURE 14.13   (A) Velocity of different body wave and guided-wave modes normalized by the bulk shear wave velocity as a function of normalized frequency, where $\omega_c = \kappa/Z$. (B) Normal or shear stiffness as a function of fracture length scale. The values in red represent ω/ω_c for these data points. *Source: Data adapted from Worthington, M., 2007. The compliance of macrofractures. Leading Edge 26, 1118−1122.*

function of normalized ω. These modes have an optimal range of ω/ω_c for the detection of fractures when $0.03 < \omega/\omega_c < 30$, and the existence of a fracture will be evident from the velocity. Reexamining the data, estimates of ω/ω_c (red numbers in Fig. 14.13A) for the laboratory and field data fall into the optimal detection range. For a field frequency of 100 Hz assuming a seismic impedance of 1.25×10^7 kg/m²s, fractures with $10^8 < \kappa < 10^{11}$ Pa/m could be detected and interpreted for fracture specific stiffness. At a typical laboratory frequency of 1 MHz for the same rock type, interpretation of fracture specific stiffness would be limited to fractures of $10^{12} < \kappa < 10^{15}$ Pa/m. This suggests that for any selected frequency, some subset of discontinuities will be optimal for detection, because different wavelengths sample different subsets of fractures.

By monitoring changes in ω/ω_c for known regions of fractures during CO_2 injection and storage process, changes in fracture specific stiffness can be inferred and linked to changes in flow. As noted by Pyrak-Nolte et al. (2016), using broadband methods in the field also can identify fractures and interpret fracture specific stiffness (e.g., Nolte et al., 2000) because the time delay (i.e. velocity) is a function of frequency (i.e. velocity dispersion). The use of broadband interpretation methods helps identify the length scales contained in a system and helps identify the elastic scattering regime.

Future Needs Related to Carbon Storage

The extended flow−stiffness relationship presented in this chapter is easily adapted to elastic rock across different moduli because, for the same fracture geometry, the elastic moduli only

contribute a prefactor to the stiffness part of the relationship that is composed of the ratio of the Young moduli when comparing two different rock types (Pyrak-Nolte and Nolte, 2016). Recommendations for future research related to caprocks include extending the flow—stiffness relationship to nonelastic rocks and to mixed mineralogy fracture—matrix systems (matrix and asperities that have different elastic moduli, such as in calcite-filled fractures in shale). Shale and other caprocks at CO_2 subsurface storage sites often display viscoelastic or plastic behavior when subjected to stress or alterations from fluid interactions that can cause swelling of the matrix and closure of fractures, as well as other time-dependent behavior (Sone and Zoback, 2014). The plasticity or viscoelasticity arises from the presence of clay minerals and organic matter (Gale et al., 2014). In some cases, fractures in shale and mudstone have a tendency to self-seal under high compressive stresses when the clay (phyllosilicate) fraction by mass is 1/3 (see Bourg, 2015). Viscoelastic and plastic deformation would require time-dependent models to determine the deformation of the asperities and the matrix. It is expected that, even with viscoelastic or plastic material properties, as a fracture self-sealed, the stiffness of the fracture would increase, fluid flow would cease, and seismic wave transmission and velocity would also increase. The viscoelastic or plastic behavior may change the functional form of the flow—stiffenss relationship, but the general behavior, i.e. flow increasing with decreasing stiffness, is expected to hold. Additional research is needed to verify this hypothesis.

Another new direction would be to extend this analysis to include shear stiffness. The normal stiffness as a function of stress does not provide direct information on flow anisotropy if it is only measured on one scale. In this study, fracture specific stiffness as a function stress exhibits similar behavior for all scales when the fracture aperture distribution is isotropic, but this is not the case for anisotropic flow. Anisotropic flow can arise from chemical alterations of a fracture (Noiriel et al., 2011; Szymczak and Ladd, 2004; Elkhoury et al., 2013; Ameli et al., 2014) and also from shearing along fractures (Gentier et al., 1997; Koyama et al., 2006), which may occur during CO_2 injection (Cappa and Rutqvist, 2011). Using elastic wave methods to measure shear stiffness may provide a means for delineating flow anisotropy. The anisotropy in aperture distribution could be studied by using two orthogonally polarized shear waves to interpret shear fracture specific stiffness for orthogonal directions. From experimental studies on fractures under shear stress in the elastic regime, normal and shear fracture specific stiffness vary in magnitude but share the same trend with stress (Pyrak-Nolte et al., 1990b; Choi et al., 2014). Other numerical studies have shown that low shear stiffness, determined from simulation of shear deformation, coincides with the direction of highest fracture conductivity (Morris, 2015). Thus it is hypothesized that shear stiffness may also probe changes in the void volume of fractures, although this hypothesis needs to be tested.

Finally, future work should extend these ideas and concepts to fracture sets and fracture networks, and to field-scale studies. Most subsurface sites do not contain a single fracture but may contain fracture zones, sets of fractures, or fracture networks. One approach for treating sets of parallel fractures or fracture networks in isotropic and anisotropic media is to use a compliance tensor (inverse of the stiffness tensor) that represents the excess compliance from the fractures (inverse of fracture stiffness) that is added to the rock matrix or background compliance (e.g., Pyrak-Nolte et al., 2016; Schoenberg and Douma, 1988; Hood and Schoenberg, 1989; Diner, 2013). Interpreting changes in compressional and shear wave velocity are used to interpret changes in fracture compliance for a fractured medium. How an averaged or weighted stiffness for a network or set of fractures relates to fluid flow through fracture network requires much

additional research. In addition, it cannot be assumed that all fractures within a set or network have the same stiffness (Shao and Pyrak-Nolte, 2016), in particular in the presence of stress or pressure gradients. The work presented here is the first step on that journey.

Acknowledgments

References

Acosta-Colon, A., Nolte, D.D., Pyrak-Nolte, L.J., 2009. Laboratory-scale study of field of view and the seismic interpretation of fracture specific stiffness. Geophys. Prospect. 57, pp. 209−224.

Ambegaokar, V., Halperin, B.I., Langer, J.S., 1971. Hopping conductivity in disoerdered systems. Phys. Rev. B. 4, pp. 2612−2620.

Ameli, P., Elkhoury, J.E., Morris, J.P., Detwiler, R.L., 2014. Fracture permeability alteration due to chemical and mechanical processes: a coupled high-resolution model. Rock Mech. Rock Eng. 47, pp. 1563−1573.

Angel, Y.C., Achenbach, J.D., 1985. Reflection and transmission of elastic waves by a periodic array of cracks: oblique incidence. Wave Motion 7, pp. 375−397.

Berkowitz, B., 2002. Charaterizing flow and transport in fractured geological media: a review. Adv. Water Resour. 25, pp. 861−884.

Bond, C.E., Wightman, R., Ringrose, P.S., 2013. The influence of fracture anisotropy on CO_2 flow. Geophys. Res. Lett. 40, pp. 1284−1289.

Bourg, I.C., 2015. Sealing shales versus brittle shales: a sharp threshold in the material properties and energy technology uses of fine-grained sedimentary rocks. Environ. Sci. Technol. Lett. 2, pp. 255−259.

Brown, S.R., 1987. Fluid flow through rock joints: the effect of surface roughness. J. Geophys. Res. 92, pp. 1337−1347.

Brown, S.R., Scholz, C.H., 1985. Closure of random surfaces in contact. J. Geophys. Res. 92, pp. 1337−1347.

Cappa, F., Rutqvist, J., 2011. Modeling of coupled deformation and permeability evolution during fault reactivation induced by deep underground injection of CO_2. Int. J. Greenh. Gas Control 5 (2), pp. 336−346.

Caricione, J.M., Picotti, S., 2012. Reflection and transmission coefficients of a fracture in transversely isotropic media. Stud. Geophys. Geod. 56 (2), pp. 307−322.

Cheng, J.T., Morris, J.P., Tran, J., Lumsdaine, A., Giordano, N.J., Nolte, D.D., et al., 2004. Single-phase flow in a rock fracture: micro-model experiments and network flow simulation. Int. J. Rock Mech. Min. Sci. 41, pp. 687−693.

Choi, M.-K., Pyrak-Nolte, L.J., Bobet, A., 2014. The effect of surface roughness and mixed-mode loading on the stiffness ratio Kx/Kz for fractures. Geophysics 79 (5), pp. D319−D331.

Cook, N.G.W., 1992. Natural joints in rock: mechanical, hydraulic, and seismic behavior and properties under normal stress. Int. J. Rock Mech. Min. 29, pp. 198−223.

De Basabe, J.D., Sen, M.K., Wheeler, M.F., 2011. Seismic wave propagation in fractured media: a discontinuous Galerkin approach. Extended Abstract. Society of Exploration Geophysicists San Antonio 2011 Annual Meeting, pp. 2921−2924.

Diner, C., 2013. Decomposition of a compliance tensor for fractures and transversely isotropic medium. Geophys. Prospect. 61 (s1), pp. 409−419.

Dumbser, M., Käser, M., 2006. An arbitrary high-order Discontinuous Galerkin method for elastic waves on unstructured meshes − II. The three-dimensional isotropic case. Geophys. J. Int. 167 (1), pp. 319−336.

Elkhoury, J.E., Ameli, P., Detwiler, R.L., 2013. Dissolution and deformation in fractured carbonates caused by flow of CO_2-rich brine under reservoir conditions. Int. J. Greenh. Gas Control 16, pp. S203−S215.

Gale, J.F.W., Laubach, S.E., Olson, J.E., Eichhubl, P., Fall, A., 2014. Natural fractures in shale: a review and new observations. AAPG Bull. 98 (11), pp. 2165−2216.

Gentier, S., Lamontagne, E., Archambault, G., Riss, J., 1997. Anistropy of flow in a fracture undergoing shear and its relationship to the direction of shearing and injection pressure. Int. J. Rock Mech. Min. Sci. 34 (3−4), pp. 94e1−94e12.

Goodman, R.E., Taylor, R.L., Brekke, T.L., 1968. A model for the mechanics of jointed rock. J. Soil Mech. Found. Div. Proc. Am. Soc. Civil Eng. 94 (SM3), pp. 637−659.

Harbert, W., Daley, T.M., Bromhal, G., Sullivan, C., Huang, L., 2016. Progress in monitoring strategies for leak reduction in geologic CO_2 storage. Int. J. Greenh. Gas Control 51, pp. 260−275.

Hedayat, A., Pyrak-Nolte, L.J., Bobet, A., 2014. Seismic precursors to the shear failure of rock discontinuities. Geophys. Res. Lett. 41, pp. 5467−5475. Available from: https://doi.org/10.1002/2014GL060848.

Hood, J.A., Schoenberg, M., 1989. Estimation of vertical fracturing from measured elastic moduli. J. Geophys. Res. 94, pp. 15611−15618.

Hopkins, D.L., 1991. The Effect of Surface Roughness on Joint Stiffness, Aperture, and Acoustic Wave Propagation (Ph. D. dissertation). University of California, Berkeley, CA, USA.

Ilgen, A.G., Heath, J.E., Akkutlu, I.Y., Brybdzia, L.T., Cole, D., Kharaka, Y., et al., 2017. Shales at all scales: exploring coupled processes in mudrock. Earth Sci. Rev. 166, pp. 132−152. March 2017.

Jaeger, J.C., Cook, N.G.W., Zimmerman, R., 2007. Fundamentals of Rock Mechanics, fourth edition. Wiley-Blackwell, Oxford, 488 p.

Kendall, K., Tabor, D., 1971. An ultrasonic study of the area of contact between stationary and sliding surfaces. Proc. R. Soc. Lond. Ser. A 323, pp. 321−340.

Koyama, T., Fardin, N., Ling, J., Stephansson, O., 2006. Numerical simulation of shear-inudced flow anisotropy and scale-depepndent aperture and transmisssivity evolution of rock fracture replicas. Int. J. Rock Mech. Min. Sci. 43 (1), pp. 89−106.

Lang, P.S., Paluszny, A., Zimmerman, R.W., 2015. Hydraulic sealing due to pressure solution contact zone growth in silicaclastic rock fractures. J. Geophys. Res. Solid Earth 120, pp. 4080−4101. Available from: https://doi.org/10.1002/2015JB011968.

Lubbe, R., Sothcott, J., Worthington, M.H., McCann, C., 2008. Laboratory estimates of normal and shear fracture compliance. Geophys. Prospect. 56, pp. 239−247.

Majer, E.L., McEvilly, T.V., Eastwood, F.S., Myer, L.R., 1988. Fracture detection using P-wave and S-wave vertical seismic profiling at the Geysers. Geophysics 53 (1), pp. 76−84.

Morris, J.P., 2012. A numerical investigation of the scaling of fracture stiffness. In: Proceedings of the American Rock Mechanics Association Symposium, 24−27 June, Chicago, IL, USA.

Morris, J.P., 2015. Numerical investigation of the relationship between fracture shear compliance and conductivity anisotropy. In: Proceedings of the 49th US Rock Mechanics/Geomechanics Symposium, 28 June−1 July, 2015, San Francisco, CA, USA. ARMA 15-554.

Myer, L.R., 2000. Factures as collections of cracks. Int. J. Rock Mech. Min. Sci. 37, pp. 231−243.

Noiriel, C., Renard, F., Doan, M.-L., Gratier, J.-P., 2011. Intense fracturing and frature sealing induced by mineral growth in porous rock. Chem. Geol. 269, pp. 197−209.

Nolte, D.D., Pyrak-Nolte, L.J., 1991. Stratified continuum percolation − scaling geometry of hierarchical cascades. Phys. Rev. A 44, pp. 6320−6333.

Nolte, D.D., Pyrak-Nolte, L.J., 1997. Coexisting two-phase flow in correlated two-dimensional percolation. Phys. Rev. E 56, pp. 5009−5012.

Nolte, D.D., Pyrak-Nolte, L.J., Beachy, J., Ziegler, C., 2000. Transition from the displacement discontinuity limit to the resonant scattering regime for fracture interface waves. Int. J. Rock Mech. Min. Sci. 37, pp. 219−230.

Oliger, A., Nolte, D.D., Pyrak-Nolte, L.J., 2003. Focusing of seismic waves by a single fractureGeophys. Res. Lett. 30 (5), 1203. Available from: https://doi.org/10.1029/2002GL016264.

Petrovitch, C.L., 2013. Universal Scaling of Flow-Stiffness Relationship in Weakly Correlated Fractures (Ph.D. dissertation). Purdue University, IN, USA.

Petrovitch, C., Pyrak-Nolte, L.J., Nolte, D.D., 2013. Scaling of fluid flow versus fracture stiffness. Geophys. Res. Lett. 40 (10), pp. 2076−2080. Available from: https://doi.org/10.1002/grl.50479.

Pollak, M.A., 1972. A percolation treatment of dc hopping conduction. J. Non-Crystall. Solids 11, pp. 1−24.

Pyrak-Nolte, L.J., Cook, N.G.W., 1988. Fluid percolation through single fractures. Geophys. Res. Lett. 15 (11), pp. 1247−1250.

Pyrak-Nolte, L.J., Morris, J.P., 2000. Single fractures under normal stress: the relation between fracture specific stiffness and fluid flow. Int. J. Rock Mech. Min. Sci. Geomech. Abstr. 37, pp. 245–262.

Pyrak-Nolte, L.J., Nolte, D.D., 1992. Frequency dependent fracture specific stiffness. Geophys. Res. Lett. 19 (3), pp. 325–328.

Pyrak-Nolte, L.J., DePaolo, D.J., 2015. Controlling subsurface fractures and fluid flow: a basic research agenda. In: DOE Roundtable Report, 2015. U.S. Department of Energy, Office of Science, Germantown, MD, USA.

Pyrak-Nolte, L.J., Nolte, D.D., 2016. Approaching a universal scaling relationship between fracture stiffness and fluid flow. Nat. Commun. 7, 10663.

Pyrak-Nolte, L.J., Myer, L.R., Cook, N.G.W., 1990a. Anisotropy in seismic velocities and amplitudes from multiple parallel fractures. J. Geophys. Res. 95 (B7), pp. 11345–11358.

Pyrak-Nolte, L.J., Myer, L.R., Cook, N.G.W., 1990b. Transmission of seismic waves across natural fractures. J. Geophys. Res. 95 (B6), pp. 8617–8638.

Pyrak-Nolte, L.J., Abell, B.C., Shao, S., 2016. Elastic wave propagation in fractured anisotropic media. In: Feng, X.-T. (ed.), Rock Mechanics and Engineering Volume 1: Principles. CRC Press, London, pp. 323–361.

Rutqvist, J., Tsang, C.-F., 2002. A study of caprock hydromechanical changes associated with CO_2 – injection into a brine formation. Environ. Geol. 42, pp. 296–305.

Schoenberg, M., 1980. Elastic wave behavior across linear slip interfaces. J. Acoust. Soc. Am. 5 (68), pp. 1516–1521.

Schoenberg, M., Douma, J., 1988. Elastic wave propagation in media with parallel fractures and aligned cracks. Geophys. Prospect. 36, pp. 571–590.

Shao, S., Pyrak-Nolte, L.J., 2016. Elastic wave propagation in isotropic media with orthogonal fracture sets. Rock Mech. 49 (10), pp. 4033–4048. Available from: https://doi.org/10.1007/s00603-016-1084-z.

Shao, S., Petrovitch, C.L., Pyrak-Nolte, L.J., 2015. Special Publications Wave Guiding in Fractured Layered Media. Fundamental Controls on Fluid Flow in Carbonates, 406. Geological Society, London, pp. 375–400.

Sone, H., Zoback, M.D., 2014. Time-dependent deformation of shale gas reservoir rocks and its long-term effect on the in situ state of stress. Int. J. Rock Mech. Min. Sci. 69, pp. 120–132.

Szymczak, P., Ladd, A.J.C., 2004. Microscopic simulations of fracture dissolution. Geophys. Res. Lett. 31, L23606.

Verdon, J.P., Kendall, J.-M., Stork, A.L., Chadwick, R.A., White, D.J., Bissell, R.C., 2013. Comparison of geomechanical deformation induced by megaton-scale CO_2 storage at Sleipner, Weyburn, and In Salah. Proc. Natl. Acad. Sci. U.S.A. 110 (30), pp. E2762–E2771.

Witherspoon, P.A., Wang, J.S., Iwai, K., Gale, J.E., 1980. Validity of cubic law for fluid flow in a deformable rock fracture. Water Resour. Res. 16 (6), pp. 1016–1024.

Worthington, M., 2007. The compliance of macrofractures. Leading Edge 26, pp. 1118–1122.

Ye, R., Petrovitch, C.L., de Hoop, M., Pyrak-Nolte, L.J., Wilcox, L., Situ, Y., 2016. A discontinuous Galerkin method with a modified penalty flux for the propagation and scattering of acoustic-elastic waves. Geophys. J. Int. 205 (2), pp. 1267–1289. Available from: https://doi.org/10.1093/gji/ggw070.2016.

Zimmerman, R.W., Kumar, S., Bodvarsson, G.S., 1991. Lubrication theory analysis of the permeability of rough-walled fractures. Int. J. Rock Mech. Min. Sci. Geomech. Abstr. 28, pp. 325–331.